Experiments in Fluids (2023) 64:110
https://doi.org/10.1007/s00348-023-03649-0

RESEARCH ARTICLE

Upper part-load instability in a reduced-scale Francis turbine: an experimental study

Ali Amini[1] · Elena Vagnoni[1] · Arthur Favrel[2] · Kazuhiko Yamaishi[3] · Andres Müller[1] · François Avellan[1]

Received: 31 January 2023 / Revised: 22 April 2023 / Accepted: 26 April 2023 / Published online: 27 May 2023

Abstract

Francis turbines with medium or high specific speeds may experience a particular type of instability in the upper part load in which the precessing vortex has an elliptical shape. The occurrence of the upper part-load instability (UPLI) is accompanied by large-amplitude pressure fluctuations at a distinct frequency between 2 and 4 times the runner rotational speed. This paper experimentally investigates UPLI for a reduced-scale Francis turbine. To investigate the causal factors of this instability, draft tube pressure measurements, particle image velocimetry, and high-speed flow visualizations have been performed at several operating points under cavitation and cavitation-free conditions. It is shown for the first time that for an operating point within the UPLI range, the vortex always features a circular section in cavitation-free conditions, which is preserved even after the initial appearance of cavitation. It is only below a certain Thoma number that the vortex section turns into an ellipse and shows an abrupt increase in pressure fluctuations. Analysis of the phase-averaged velocity fields reveals that a concentrated vortex with a large precession radius is a prerequisite for UPLI, while the instantaneous velocity fields clearly illustrate the asymmetric velocity distribution around the elliptical vortex. The existence of a breathing mode and the intermittent formation of two side vortices along the elliptical vortex rope are also evidenced by high-speed flow visualizations. These results provide a much deeper insight into the flow structures that favor the development of UPLI and help delimit its thresholds to higher precision, and thus, prevent its occurrence during turbine operations.

1 Introduction

As of 2020, hydropower is the largest source of low-carbon energy accounting for about 60% of the renewable production and for almost 16% of the global electric production. Besides their important generation capacities, hydropower plants have traditionally played a key role in grid resilience by providing fast transitions and ancillary services accounting for nearly a third of the world's capacity for flexible electricity supply. With the current decarbonization plans and the massive integration of intermittent renewable energy sources, such as wind and solar, even higher levels of flexibility are required from the hydropower sector, which translates to more frequent startups and shutdowns, faster transition regimes, and more time spent in off-design conditions. These maneuvers result in problems such as efficiency drops, cavitation, hydro-acoustic resonances, and flow instabilities, which, in turn, lead to pressure fluctuations, vibrations, noise, fatigue, and premature wear of the components (Favrel et al. 2019a; Gomes Pereira et al. 2022; Goyal and Gandhi 2018; Kougias et al. 2019).

Francis turbines are the most widely used type of hydropower turbines and account for about 60% of the installed capacity worldwide. These turbines can be operated over a wide range of discharge and head variations. However, depending on the operating regime, different phenomena may arise within a Francis turbine including, but not limited to, the formation of inter-blade vortices for deep part load (Wack and Riedelbauch 2015; Yamamoto et al. 2017), a precessing vortex rope in the draft tube for part load (Favrel et al. 2016; Goyal et al. 2017a; Li et al. 2021), and a self-oscillating cavitation vortex for full load (Müller et al. 2017; Zhao et al. 2021). Cavitation is another common consequence of operating a Francis turbine far from its best efficiency point (BEP) and can lead to structural vibration,

✉ Ali Amini
ali.amini@alumni.epfl.ch

[1] Laboratory for Hydraulic Machines, École Polytechnique Fédérale de Lausanne (EPFL), Lausanne, Switzerland

[2] Hydro-Québec Research Institute (IREQ), Hydro-Québec, Varennes, QC, Canada

[3] Power & Digital Business Unit, Nippon Koei Co., Ltd., Sukagawa 962-8508, Japan

performance degradation, and mechanical damage due to erosion (Avellan 2004; Escaler et al. 2006; Sreedhar et al. 2017; Arabnejad et al. 2020). Numerous studies have contributed to understanding the cavitation physics (Teran et al. 2018; Amini et al. 2019a; Gawandalkar and Poelma 2022) and to developing counter-measures to mitigate its adverse effects in hydraulic machines (Rivetti et al. 2015; Amini et al. 2019c; Joy et al. 2022; Khullar et al. 2022).

The part-load vortex rope has a precession frequency (f_{rope}) between 0.2 and 0.4 times the runner rotational frequency and induces significant pressure pulsations and vibrations. This phenomenon has been the topic of several studies and various techniques have been proposed for mitigating its side effects (Favrel et al. 2015; Goyal et al. 2017b; Pasche et al. 2018, 2019a). Another important but less common form of instability that may develop in the part load regime is the so-called upper part-load instability (UPLI). This instability can occur for between 70 and 85% of the nominal discharge (Nicolet et al. 2010) and is associated with the transformation of the cross section of the part-load vortex rope from a circle to an ellipse. UPLI occurs only in medium- and high-specific-speed Francis turbines (Koutnik et al. 2006) and is accompanied with pressure fluctuations of much larger amplitude compared to the normal vortex rope, emitted at a distinct frequency (f_{upper}) in the range of 2–4 times the runner rotational frequency (Fisher et al. 1980; Dörfler 1994; Nicolet et al. 2010). Koutnik et al. (2006) show that, for a given section, these fluctuations are in phase and synchronous. This instability causes severe vibrations and impacts the performance and lifespan of the machine.

Since the vortex rope has an elliptical shape, Koutnik et al. (2006) and Kirschner et al. (2009) attribute the high-frequency pressure pulsations of the UPLI to the self-rotation of the elliptical vortex rope, which develops a self-rotating asymmetric pressure distribution. In contrast, Nicolet et al. (2010) suggest that a self-sustaining breathing pattern may form in the cavitation volume within the draft tube, which induces the observed pressure pulsations. In a numerical study, Alligné et al. (2011) assert that the root cause of this phenomenon is an instability in the cavitation volume that fluctuates at a frequency matching one of the eigenfrequencies of the hydraulic system. In two complementary experimental and analytical studies (Dörfler 2019a, b), Dörfler demonstrates that the UPLI pulsations are self-excited, meaning that at least one eigenvalue of the hydraulic system becomes unstable. He also notes that all the instabilities of this class are "breathing" pulsations and synchronous within one cross section. This implies that there is no phase lag between wall pressure measurements realized at different azimuthal locations on a cross section of the draft tube at a given distance from the runner outlet, which is in contrast with the pressure variations due to the passage of the precessing vortex.

Applying a phase shift analysis on the data gathered from 104 pressure transducers installed along the draft tube of a model Francis turbine, Arpe et al. (2009) show that the location of the excitation source is in the elbow and the emitted hydrodynamic waves propagate in both upstream and downstream directions. Pasche et al. (2019b) investigate the origin of these synchronous pressure waves in a Francis turbine with a simplified axisymmetric draft tube. Applying a Fourier series decomposition of the 3D flow field and using asymptotic expansions, they show that the synchronous pressure wave is amplified in the downstream direction and travels back upstream toward the turbine runner. They argue that for a real draft tube geometry, the disturbance that triggers the instability is the point where the vortex rope hits the elbow. In an experimental study, Favrel et al. (2019b) investigate this phenomenon in a model of a Francis turbine by means of two cameras to obtain a realistic estimation of the cavitation volume in the draft tube. Although not able to either confirm or refute the existence of a breathing mode, they found intermittent central collapses within the elliptical vortex rope, which lead to the development of two distinct cavities on the two sides of the elliptical vortex rope. Amini et al. (2021) highlight the influence of the Thoma number on the initiation and development of UPLI and shed light on the velocity field variations at the vicinity of the elliptical vortex. In a recent study, Favrel et al. (2022) develop a simplified analytical model of a cavitation vortex and demonstrate that the ellipticity of the vortex cross section and the amplitude of its oscillations are directly correlated with the amplitude of the UPLI pressure fluctuations.

Since UPLI occurs at discharge values quite close to the BEP, determining the instability thresholds is a crucial step to avoid undesired pressure fluctuations and structural vibrations. Even though several authors have elaborated on the topic, there exists no consensus on the origin of this instability and its impacts on the flow structures in the draft tube. The present paper aims at answering these questions by performing an experimental study on the occurrence and development of UPLI. To this end, draft tube pressure measurements, particle image velocimetry (PIV), and high-speed flow visualizations have been deployed for several operating points in cavitation and cavitation-free conditions. The details of the experimental setup and post-processing methods are described in Sect. 2. The results and analyses are presented in Sect. 3, which include an analysis of the pressure measurements in the time and frequency domains, the effect of the Thoma number on the cavitation vortex rope shape, and velocimetry results for both cavitation and cavitation-free vortex ropes at various discharges. Lastly, a discussion on the root causes of UPLI is provided in Sect. 4 followed by a conclusion in Sect. 5.

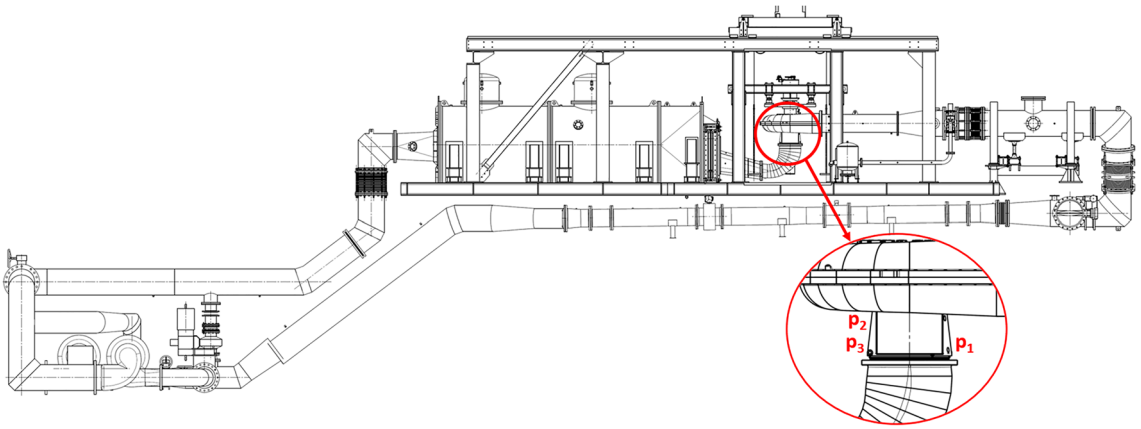

Fig. 1 Schematic of the PF3 test rig of EPFL with the three pressure sensors installed on the draft tube wall

2 Experimental setup

The experiments are performed with a reduced-scale Francis turbine installed on test rig PF3 of the Technology Platform for Hydraulic Machines at EPFL. The reduced-scale model has an upstream inlet pipe, a spiral case, a runner with a reference outlet diameter of $D = 0.35$ m, and a draft tube consisting of a cone, an elbow, and a diffuser. The tested turbine has a specific speed $\nu = 0.33$ defined by:

$$\nu = \frac{\omega Q^{1/2}}{\pi^{1/2}(2E)^{3/4}}, \tag{1}$$

where ω is the runner rotational speed [rad/s], Q is the turbine discharge [m^3/s], and E is the specific energy [J/kg]. The hydraulic power injected into the closed-loop test rig is provided by two parallel 300-kW centrifugal pumps. The amount of the specific hydraulic energy in the circuit is determined by the rotational speed of the pumps while the discharge is regulated by the guide vanes opening of the turbine, and the rotational speed of the runner is controlled by a 300-kVA DC generator. According to International Electrotechnical Commission standards (Standard 1999) the operating conditions of a hydraulic machine are characterized by the following non-dimensional parameters: speed factor (n_{ED}), discharge factor (Q_{ED}), Froude number (Fr), and Thoma number (σ), which are defined by:

$$n_{ED} = \frac{nD}{\sqrt{E}}, \; Q_{ED} = \frac{Q}{D^2\sqrt{E}}, \; Fr = \sqrt{\frac{E}{gD}}, \; \sigma = \frac{\mathrm{NPSE}}{E}, \tag{2}$$

where n is the rotational speed of the runner [Hz], g is the acceleration due to gravity, and NPSE is the net positive suction specific energy, which is defined by:

$$\mathrm{NPSE} = \frac{p_0 - p_v}{\rho} + g\left(z_0 - z_{\mathrm{ref}}\right) + \frac{C_{\mathrm{out}}^2}{2}, \tag{3}$$

where p_0 and z_0 are the static pressure and the level of the downstream tank, respectively, p_v is the saturation vapor pressure at the water temperature, z_{ref} is the reference level of the machine centerline, and C_{out} is the average fluid velocity at the draft tube outlet (discharge value divided by the cross section area). The BEP of the turbine is characterized by the following: $n_{ED@\mathrm{BEP}} = 0.343$ and $Q_{ED@\mathrm{BEP}} = 0.220$. In the experiments, the speed factor was kept constant at its nominal value and the discharge factor was varied in the part-load regime by changing the discharge. The value of σ was controlled by changing the static pressure in the downstream tank via a vacuum pump. Unless otherwise specified, the measurements were performed at nominal Froude number (i.e., Fr = 7.75). It is worth mentioning that the measurement uncertainties of the discharge, pressure, and the Thoma number are $\pm 0.20\%$, $\pm 0.15\%$, and $\pm 1\%$, respectively.

A schematic of the test rig is shown in Fig. 1. Three flush-mounted piezo-resistive pressure sensors are installed at the cone wall of the draft tube. Sensor p_2 is $0.3D$ downstream of the runner whereas sensors p_1 and p_3 are installed farther downstream at $0.85D$ below the runner outlet. Sensors p_2 and p_3 are geometrically in phase whereas sensor p_1 is at 180° from them. These sensors have an absolute pressure range of 0–5 bars with a maximum relative error of 0.7%. Their sampling frequency is set to 1 kHz during the experiments. For each sensor, the pressure coefficient $[C_p = \left(p - p_{\mathrm{avg}}\right)/\rho g H]$ is computed by comparing the instantaneous pressure (p)

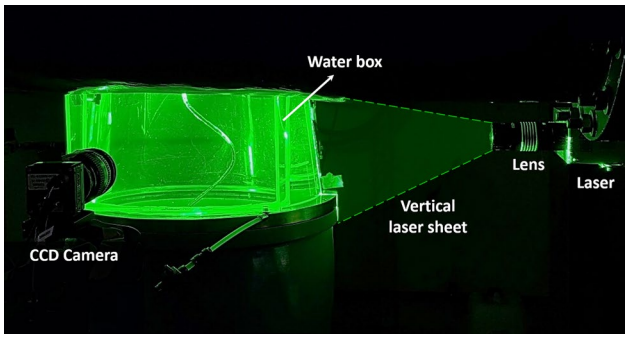

Fig. 2 Photograph of the cavitation vortex rope in the transparent draft tube illuminated by the PIV laser

with the mean pressure of that measurement (p_{avg}) and normalizing it by the net head (H) of the turbine.

To provide visual access to the flow, the upper part of the draft tube is manufactured from transparent Plexiglas. This allows us to perform optical experiments, such as visualizing the cavitation flow and making PIV measurements. To avoid light distortion due to the curved surface of the draft tube, a rectangular water box is attached to it on one side. The box is filled with degassed water to avoid nucleation on its walls. Figure 2 is a photograph of the draft tube cone with the water box installed. This photograph was taken during meridional PIV measurements in the part-load regime and illustrates the cavitation vortex rope in the draft tube illuminated by the vertical laser sheet. As it is shown in Fig. 2, setting the camera objective parallel to the water box face allows for a complete neutralization of the light refractions due to the curvature of the draft tube wall.

High-speed flow visualizations of the cavitation vortex rope at part-load conditions are achieved with a Photron FastCam Mini 200 camera at image acquisition rates of up to 10 000 frames per second and a resolution of 1024 × 1024 pixels. A 90% uniform LED screen (PHLOX LEDW-BL-550X400-MSLLUB-Q-1R-24 V) of size 500 × 400 mm and 7000 cd/m^2 luminescence is installed as a backlight source to enhance the contrast between the gaseous and liquid phases. The illumination is improved by two 800-W continuous lights installed at the front and side.

To obtain a better insight into the flow structures in the draft tube cone, 2D planar PIV measurements are performed on two horizontal cross sections and one meridional plane in the draft tube. A double-pulse 200-mJ Nd:YAG laser with a cylindrical lens illuminates the measurement planes and images are captured with a CCD camera. Figure 3 shows a schematic of the experimental setup with the measurement planes as well as the visual access through the elbow and the camera position for the upper and lower horizontal planes of measurement. To avoid unwanted reflections from the pressure transducers, the PIV planes are slightly off the pressure sensor planes. Namely, the upper PIV plane is at 0.2D from the runner outlet and the lower plane is at 0.75D from the runner outlet.

Fluorescent particles are used for the PIV tests over a wide range of flow conditions, including cavitation flows, which is not feasible with normal particles due to the extensive light reflections from the cavity interfaces. The particles are prepared in the laboratory based on the recipe available in Müller et al. (2013). The spherical polyamide particles used have an average diameter of 20 µm and are dyed with rhodamine 6G. This fluorescent dye absorbs laser light at 532 nm and emits light between 570 and 660 nm with a

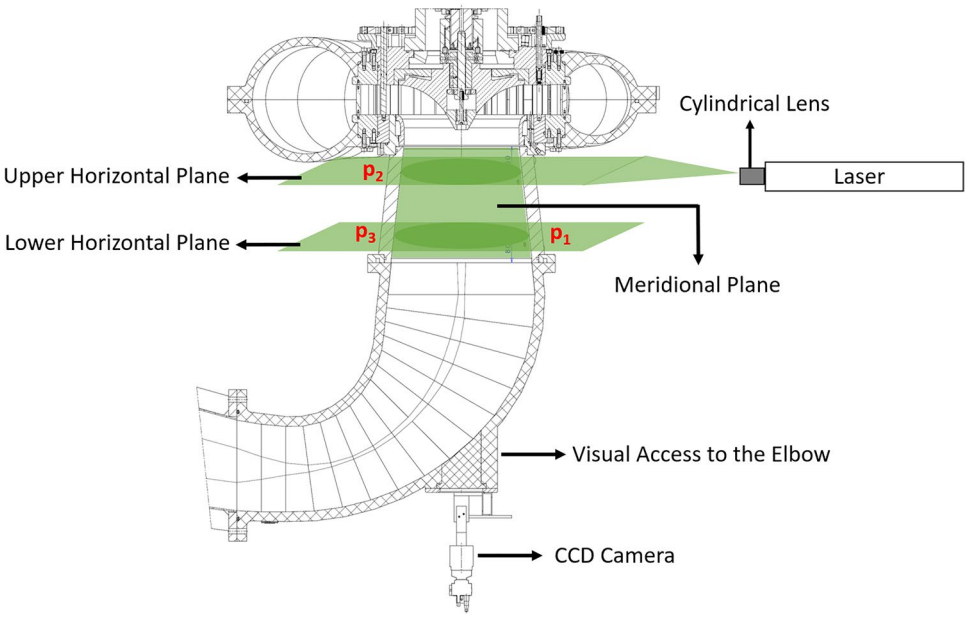

Fig. 3 Schematic of the PIV setup showing the three measurement planes and the pressure sensor locations

maximum intensity at 590 nm. An orange filter is installed in front of the camera so that unwanted reflections from the cavity surface are eliminated and only the orange light reflected from the particles reaches the camera sensor.

For each operating condition, 10,000 image pairs are acquired at a rate of 10 image pairs per second. This number is sufficiently large such that the phase-averaged results are statistically independent from the number of samples. To calculate the velocity field from the acquired images, each image is first de-warped, meaning that it is compared to a calibration image of the same view. Thereafter, each pixel is assigned to the corresponding physical coordinates. In the next step, a mask is applied to the images to remove the out-of-interest regions. This includes the near-wall region, which contains a considerable number of spurious vectors due to the light reflections from the wall. The final step is to apply the cross-correlation PIV algorithm (with 50% overlap in both directions) to each pair of successive images to find the instantaneous velocity fields. To accelerate the calculations, the velocity components are initially computed on interrogation areas of 64×64 pixels, which are ultimately refined to windows of 16×16 pixels. These windows correspond to a physical vector-to-vector resolution of around 3.2×3.2 mm, the exact size of which depends on the measurement plane of interest. The time difference between two successive frames is tuned at 200 µs in the experiments. This value is selected such that the particles displacement remains inferior to one third of the interrogation windows size. To evaluate the measurement errors, an uncertainty of 0.1 pixels is assumed in the measurement of the particle displacements as in (Dreyer et al. 2014). In our experiments, the average particle displacement is about 2.3 pixels on the horizontal planes and 3.1 pixels on the vertical plane. Thus, the uncertainty associated with the calculation of the velocity vectors is estimated to be around 4.3% and 3.3% on the two horizontal planes and the vertical plane, respectively. To remove the remaining spurious vectors from the results in the not-masked central region, a range filter, and then, a moving average filter with a 3×3 neighborhood and an acceptance factor of 0.15 are applied to the velocity fields. It is noteworthy that the number of spurious vectors does not exceed 5% of the total population.

2.1 PIV post-processing

As the experiments are performed in the part-load regime, the flow in the draft tube is driven by the precession of the vortex rope, which has a periodic behavior with an almost constant frequency, f_{rope}. This necessitates the application of phase averaging as presented in Favrel et al. (2015); thus, the pressure signal is selected as the reference. For a given cross section, the passage of the vortex rope in front of a pressure sensor induces a drop in the measured pressure. Therefore, each pair of successive minima in the pressure signal represents a complete revolution of the vortex rope in that section. The relative distance of a given point to its preceding minimum is used to determine the revolution phase. Concretely, the wall pressure and PIV trigger signals are recorded synchronously. The pressure signal is first filtered (low pass filter and moving average) to smooth down its high-frequency fluctuations. A minimum detection algorithm is applied to the filtered signal to determine the exact location of the pressure minima. Each PIV instance is labeled with the revolution phase based on the relative distance of its trigger signal to its adjacent pressure minima. The procedure is illustrated in Fig. 4. Ultimately, the instantaneous velocity fields obtained for a given operating condition are phase-averaged over all the measured instants based on the assigned phase labels. In this work, a total of 100 phases are considered. Thus, each phase represents 3.6° of one whole revolution of the vortex rope.

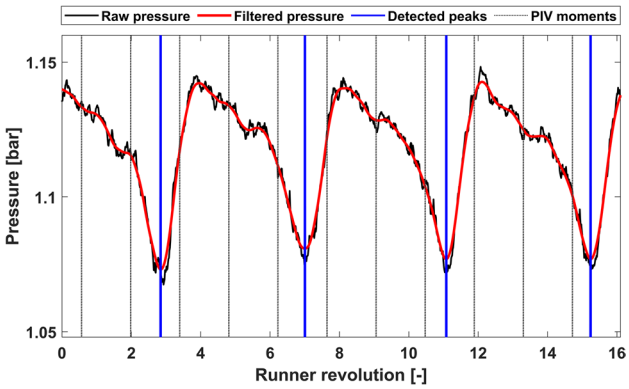

Fig. 4 Results of the minimum pressure detection algorithm and phase labels for PIV images

The phase-averaged velocity fields are subsequently analyzed to extract quantitative information. These analyses included determining the vortex precession radius, extracting its intensity, and finding its tangential velocity profile, and thereby, its viscous core radius. The first step is to determine the vortex center location and delimit the vortex boundaries. For this purpose, the methods developed by Graftieaux et al. (2001) are adopted. These authors introduce two non-dimensional scalars Π_1 and Π_2:

$$\Pi_1(P) = \frac{1}{N} \sum_S \frac{(\mathbf{PM} \times \mathbf{C}(M)) \cdot \mathbf{z}}{\|\mathbf{PM}\| \cdot \|\mathbf{C}(M)\|}, \tag{4}$$

$$\Pi_2(P) = \frac{1}{N} \sum_S \frac{(\mathbf{PM} \times (\mathbf{C}(M) - \mathbf{C}(P))) \cdot \mathbf{z}}{\|\mathbf{PM}\| \cdot \|\mathbf{C}(M) - \mathbf{C}(P)\|}, \tag{5}$$

where P and M are two arbitrary points within the rectangular domain S, which has a fixed size of N points. $\boldsymbol{PM}$ is the vector connecting the two points, $\mathbf{C}(M)$ and $\mathbf{C}(P)$ are the velocity vectors at points M and P, respectively, and $\mathbf{z}$ is the unit vector normal to the plane of the rectangular domain. Once these two values are computed for a 2D velocity field, the location where Π_1 is maximum shows the center of the vortex and the area where $|\Pi_2|$ is larger than $2/\pi$ specifies its boundaries. The advantage of this method is that the detected boundaries can have any arbitrary shape depending on the velocity field. These methods have been successfully implemented by different authors with applications such as detecting vortex centers and making a wandering correction of tip trailing vortices (Dreyer et al. 2014; Amini et al. 2019b) as well as for phase-averaging and evaluating vortex ropes in Francis turbines (Favrel et al. 2015). In the present work, to accelerate the computation, Π_1 is first calculated on a down-sampled velocity field (by a factor of 5) to quickly detect the approximate position of the vortex center. In the second step, the original fine mesh is restored around this area and the algorithm is applied again to compute the exact location of the vortex center. Once the center of the vortex is found, Eq. (5) is used to precisely determine its boundaries. When the vortex boundaries are found, its circulation (Γ) can be calculated with both curvilinear and surface integrals shown in Eq. (6):

$$\Gamma = \oint_l \mathbf{C} \cdot d\mathbf{l} = \int_S \omega_z \mathbf{dS}. \tag{6}$$

The curvilinear integral uses the inner product of the velocity vector ($\boldsymbol{C}$) along the contour of the vortex boundary whereas the surface integral requires that the out-of-plane vorticity (ω_z) is computed in advance. The normal component of vorticity at a given point is defined by:

$$\omega_z = \frac{\partial C_y}{\partial x} - \frac{\partial C_x}{\partial y}, \tag{7}$$

where C_x and C_y are the x and y components of the velocity at that point. To compute this variable, a five-point centered numerical scheme is implemented for both directions:

$$\begin{aligned}\omega_{i,j} = &\frac{1}{12\Delta X}\left(-v_{i+2,j} + 8v_{i+1,j} - 8v_{i-1,j} + v_{i-2,j}\right) \\ &- \frac{1}{12\Delta Y}\left(-u_{i,j+2} + 8u_{i,j+1} - 8u_{i,j-1} + u_{i,j-2}\right).\end{aligned} \tag{8}$$

In Eq. (8), i, j, u, v, ΔX, and ΔY are the indices, velocity components, and the grid sizes in the x and y directions, respectively. This methodology is applied to each phase individually. The final values are calculated as an average over the 100 phases. To obtain the average tangential velocity fields for any given phase, the location of the vortex center is determined, and then spatial averaging is performed at 360° around this point to calculate the average tangential velocity as a function of distance from the vortex center, i.e., the vortex radius. This approach is repeated for all phases. Finally, the mean and standard deviation of the tangential velocity of the vortex are determined for the 100 velocity profiles. The results provide useful information on the viscous core radius and the maximum tangential velocity of the vortex rope for different operating conditions.

3 Results and discussion

3.1 Evidence of UPLI

Presented in Fig. 5 (left) are flow visualizations captured at $Q/Q_{\mathrm{BEP}} = 0.84$ and nominal n_{ED} for two Thoma number values: $\sigma = 0.14$ and $\sigma = 0.10$ depicted at the top and bottom, respectively. UPLI is associated with the transformation of the vortex cross section from a circle into an ellipse. This effect is well depicted in Fig. 5 (left). At the top, the vortex rope has a circular cross section and is *stable*. A slight decrease in the Thoma number from $\sigma = 0.14$ to $\sigma = 0.10$, however, triggers the UPLI. The vortex rope becomes *unstable* and holds an elliptical shape as shown at the bottom of Fig. 5 (left). When the UPLI mode is activated, in addition to the precession motion, the vortex rope undergoes self-rotation around its own axis. This drastic change in the vortex form leaves a clear fingerprint in the pressure signals measured at the draft tube wall, which are illustrated in Fig. 5 (right). As is clear, a high-amplitude and high-frequency excitation appears in the pressure signal for the unstable vortex at $\sigma = 0.10$. This excitation is associated with a distinct frequency peak between 2 and 4 times the runner frequency and results in high-amplitude noise and vibrations in the whole test rig.

3.2 Dynamics of the precessing vortex

To develop a better understanding of the UPLI, the part-load regime is first investigated in cavitation-free conditions. For this purpose, the power spectral densities of the pressure coefficients measured at the draft tube wall are calculated for different discharges. As the flow in this regime is reigned by the precession motion of the vortex rope, the dominant frequency in the resulting spectrum corresponds to the vortex precession frequency (f_{rope}), the values of which are plotted in Fig. 6 (left) as a function of the discharge. The spectral power of the pressure coefficient at f_{rope}, denoted by G_{xx}, is also plotted in Fig. 6 (middle) versus the discharge.

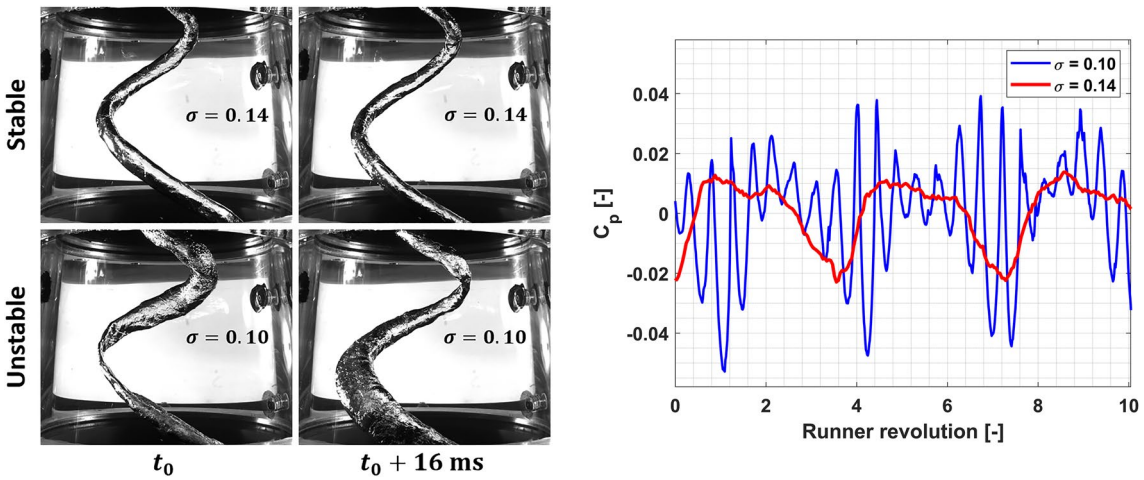

Fig. 5 Left: Comparison of a stable circular (top) and an unstable elliptical vortex (bottom). Right: Emergence of high-amplitude high-frequency oscillations in the pressure signal measured at the draft tube wall. The operating conditions correspond to nominal n_{ED} and $Q/Q_{\mathrm{BEP}} = 0.84$

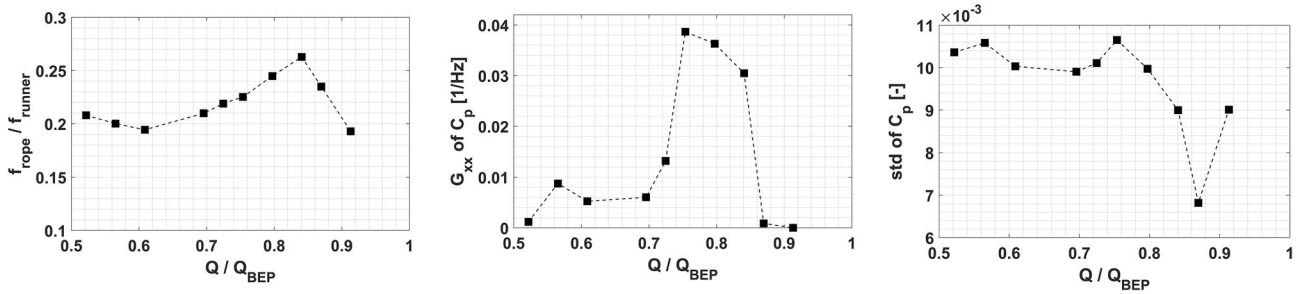

Fig. 6 Left: Normalized frequency of the precessing vortex plotted as a function of the discharge value. Middle: Spectral power of the pressure coefficient at the precession frequency. Right: Standard deviation of the pressure coefficient over the 1000 s of measurement

Moreover, the standard deviation of the pressure coefficient is depicted for the different discharge values in Fig. 6 (right).

It can be inferred from Fig. 6 (left) that for this specific machine, the vortex passage frequency is mainly between 20 and 30% of the runner frequency (f_{runner}). Above 60% of the BEP discharge, the precession frequency increases almost linearly to its highest value at $Q/Q_{\mathrm{BEP}} = 0.84$. Beyond this discharge value, f_{rope} undergoes a rapid decrease. This decline is also pronounced in Fig. 6 (middle), which shows that at around 90% of the nominal discharge, the spectral power of the precession frequency is much lower compared to that for lower discharges. In Fig. 6 (right), a similar decrease is observed at the same discharge values for the standard deviation of the pressure coefficient. These observations clearly reflect the upper bound for the formation of a coherent and strong precessing vortex in the draft tube. It can be observed that the highest values for both the precession frequency and the corresponding signal power occur between $Q/Q_{\mathrm{BEP}} = 0.75$ and 0.85. This range corresponds to the so-called upper part-load regime. It can be inferred from the results that, in this range, the vortex rope has its most coherent structure. The standard deviation of the pressure indicates that these values remain almost constant at the different discharge values. The measurements shown in Fig. 6 were performed under nominal n_{ED}.

3.3 Cavitation-free flow measurements

The pressure coefficient is plotted for different values of the turbine discharge in Fig. 7. The pressure is measured with sensors p_2 (upper plane) and p_3 (lower plane). The moment when the vortex passes each sensor corresponds to the lowest pressure and is chosen as reference. One complete revolution is divided into 100 phases. Given its relative distances from the extrema, each data point between any two successive minima in the pressure signal is attributed to a certain phase. The pressure values are then phase-averaged over the whole sample of 1000 s acquired at 1 kHz. Note that, for clarity, the lines for the standard deviations are scaled to 40% of the real values to ensure the graphs are readable.

The values of the pressure coefficient close to the runner exit (C_{p_2}) are shown in Fig. 7 (left). As is clear, close to

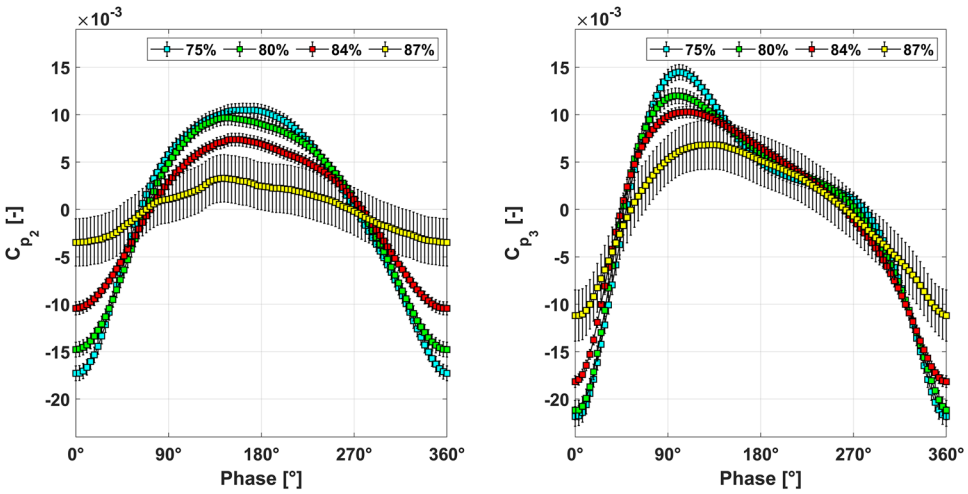

Fig. 7 Effect of the discharge value on the phase-averaged pressure at the upper (left) and lower (right) measurement planes in the draft tube at nominal n_{ED}

the BEP, the pressure coefficient measured at the draft tube wall is relatively small. The value increases in amplitude quite significantly as the discharge decreases from 87% of the BEP to 75%. Similar observations can be made regarding the pressure values from the sensor installed slightly farther downstream (C_{p_3}), as plotted in Fig. 7 (right). Close to the BEP, the amount of swirl injected into the draft tube is quite small, leading to the formation of a weak vortical flow at the center of the tube with a small precession radius, which barely influences the wall pressure. Farther from the BEP, more swirl is injected into the draft tube, and therefore, a stronger vortical flow forms. This results in a stronger vortex in terms of intensity (circulation) and probably a larger precession radius, leading to higher impacts on the wall pressure. The values of the standard deviations are notably higher for $Q/Q_{\mathrm{BEP}} = 0.87$ compared to the lower discharge values. This is probably because, at this discharge value, the vortex has a less coherent structure with a small precession radius, leading to a higher ratio of noise to periodic fluctuations.

The results presented in Fig. 7 explain how the flow develops in the draft tube. Right at the runner exit (p_2), the pressure coefficient has a symmetric profile so that the time it takes for the pressure to recede due to the vortex passage is almost equal to the time it takes to rise back. This implies that the flow around the vortex is symmetric at this horizontal plane. As the flow develops farther downstream, two differences are observed. First, the amplitude of the pressure coefficient increases drastically. This is due to an increase in the precession radius that takes the vortex closer to the wall. Second, the profile of the pressure coefficient also alters and is no longer symmetric at the lower measurement plane. In fact, it takes only 25% of a complete revolution for the pressure to rise back to its maximum after the passage of the vortex. For the rest of the cycle, the pressure decreases gradually to its minimum value. This behavior is more pronounced at $Q/Q_{\mathrm{BEP}} = 0.75$ and diminishes as the discharge increases toward Q_{BEP}. This observation is in line with previous research (Cala et al. 2006; Favrel et al. 2015) which show that as the vortex center gets closer to the wall (precession radius increases), the vortex core becomes more asymmetric, resulting in a more asymmetric pressure field.

The contours of the velocity magnitude, $C = \left(C_x^2 + C_y^2\right)^{1/2}$, along with the local velocity vectors are illustrated in Fig. 8 for four discharge values (in columns) and for the three measurement planes (in rows). For all cases, the precession is counterclockwise. The contours presented here all correspond to the same vortex revolution phase for the pressure measured at p_3. As the PIV planes are slightly off the pressure sensor planes to avoid unwanted reflections, the phase selected does not necessarily correspond to vortices at similar positions on each measurement plane. For all the cases, the circles and trapezoids drawn in bold lines depict the physical boundaries of the draft tube in each cut, whereas the dashed lines represent the areas where the PIV results are reliable (sheltered from wall reflections). The parameter R, used for nondimensionalization, is the draft tube radius at the upper plane and U is the runner circumferential velocity at the turbine exit. Also note that when making measurements on the lower horizontal plane at $Q/Q_{\mathrm{BEP}} = 0.84$, the vortex is slightly filled with cavitation despite having the same Thoma number as the upper plane. This is why the contour shown for this flow condition is marginally distorted around the vortex center.

The measurements on the two horizontal planes shown in Fig. 8 reveal that at lower discharge values, the precessing structure in the draft tube is larger and the vortical flow occupies a larger portion of the cross section compared to higher discharges. At higher discharge values, the vortex has a quite concentrated structure with a small viscous core, and therefore, does not influence the entire flow in the draft tube.

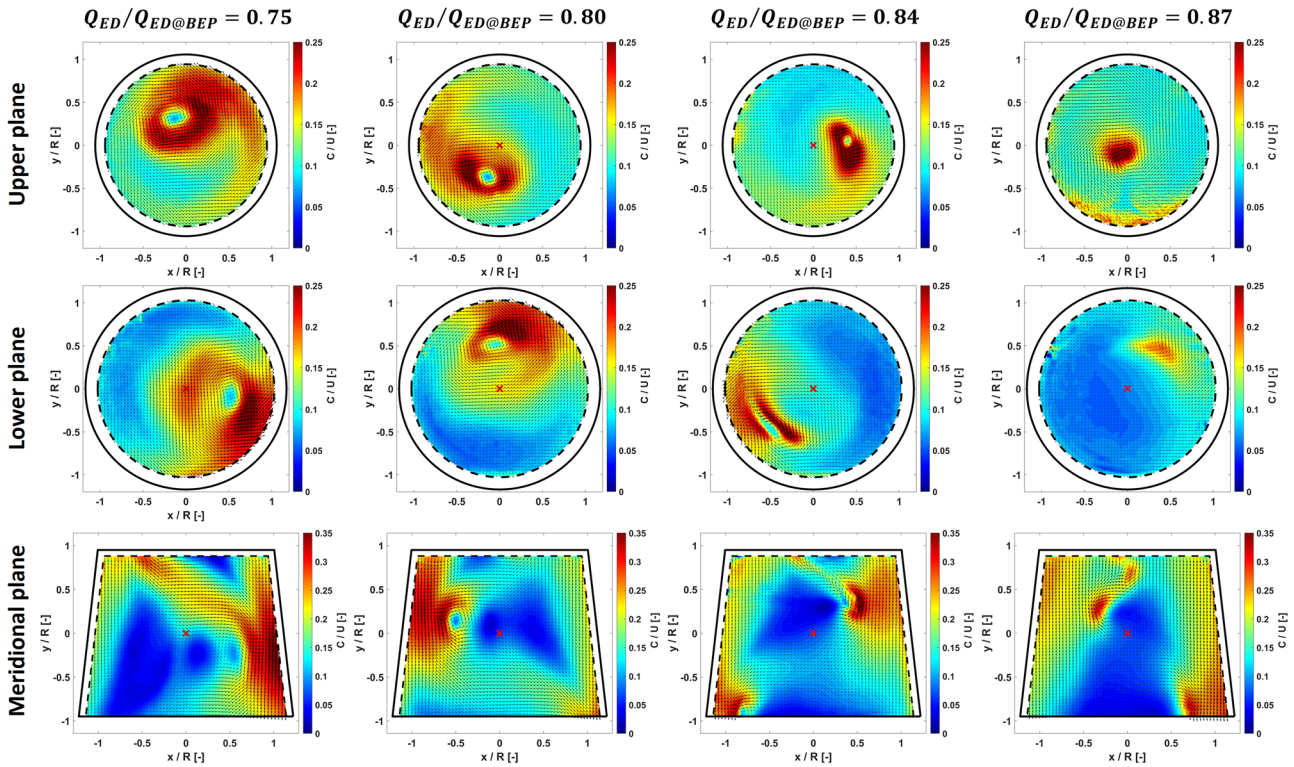

Fig. 8 Phase-averaged velocity magnitude contours on the three measurement planes for four discharges

At 75% of the nominal discharge, the precessing vortical structure occupies almost half of the cross section, whereas at 87%, the vortex is barely precessing at all on the upper plane and remains very close to the center point. Being smaller than the PIV resolution, the viscous core structure of the vortex is not fully captured for $Q/Q_{\mathrm{BEP}} = 0.87$. Despite this shortcoming, it is still evident that as the flow develops downstream at this discharge value, the vortex undergoes a helical breakdown and precesses with a relatively large radius on the lower plane. This is, though, accompanied by a noticeable decrease in the magnitude of the tangential velocity component. This observation at 87% of the BEP discharge clearly explains the C_p profiles shown in Fig. 7. On the upper plane, the vortex remains close to the center; therefore, the wall pressure is barely impacted. On the lower plane, the vortex moves closer to the wall and the pressure coefficient has a profile similar to the other discharge values, although with a smaller amplitude. Similarly, for the three other discharge values, it is observed that the vortex has a more concentrated and coherent structure close to the runner exit (upper plane), which becomes diffused as it flows downstream. As a result, a larger portion of the section is affected by the vortical flow while the magnitude of the tangential velocity decreases. The coherent structures observed in these contour plots clearly explain the high values of G_{xx} in Fig. 6 (middle) for the discharge values between 75 and 84% of the BEP. Accordingly, UPLI is primarily observed at 80% and 84% of the BEP discharge in the present experiments.

The velocity contours on the meridional plane in Fig. 8 show the interaction between the mainstream downward flow and the rotational velocity of the vortex rope at its intersections with the measurement plane. At the outer side of the intersections, the tangential velocity of the vortex and the mainstream flow are co-directional, resulting in a boosted downward flow close to the draft tube wall. The extent of this amplification increases as the discharge is reduced, which is a result of the higher tangential velocities obtained at the lower discharge values, as was observed in Fig. 8 for the horizontal planes. The opposite holds for the inner side of the intersections where the mainstream flow and the tangential velocity of the vortices are counter-directional. It can be seen in the contour plots that an almost stagnant region forms at the center of the draft tube. Examining the flow structure in phases in addition to the one presented in Fig. 8 reveals that the dead zone grows in size as the discharge decreases. This is due to the stronger vortices that form at the lower discharges, which counterbalance the mainstream more effectively and lead to a larger stagnant area at the center of the draft tube cone.

To further investigate the velocity fields, an algorithm to detect vortex centers is developed based on Graftieaux's method (Graftieaux et al. 2001). The method is applied to

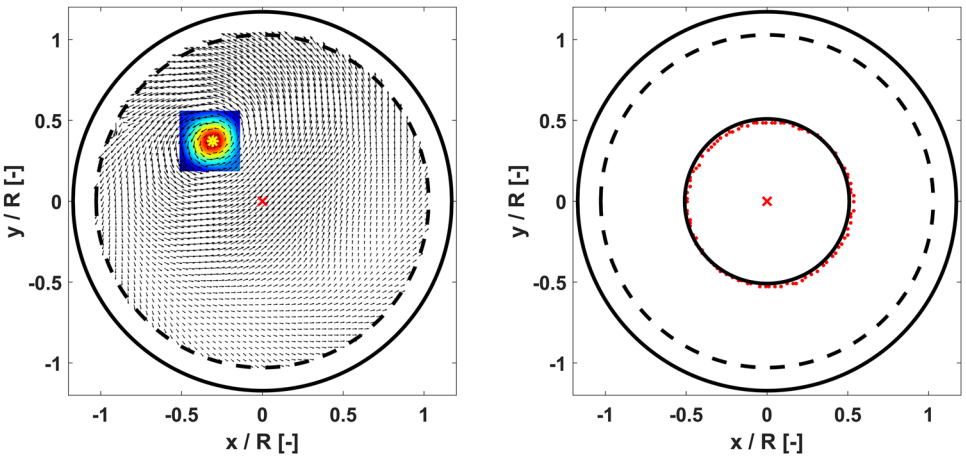

Fig. 9 Left: Detecting a vortex center with high accuracy. Right: Vortex centers detected for 100 phases along with the fitted precession trajectory

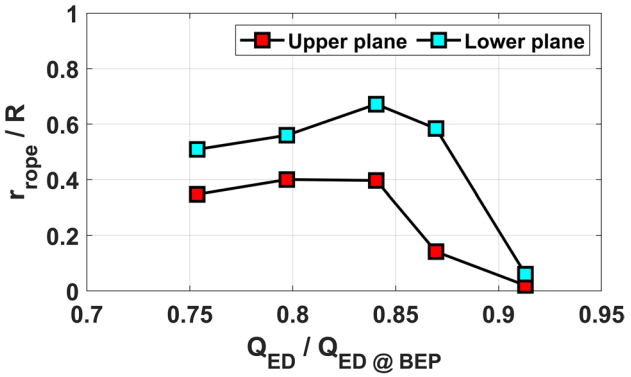

Fig. 10 Precession radius at the upper and lower planes as a function of the turbine discharge

the phase-averaged velocity contours and provides the average precession radius for each flow condition. An example of vortex center detection for a given phase is shown in Fig. 9 (left). The colored area around the vortex center is the contour of Π_1 in Graftieaux's algorithm, the maximum of which occurs at the vortex center. Executing the algorithm for all 100 phases and fitting a circle to the obtained centers provides the average precession radius (r_{rope}), which is illustrated in Fig. 9 (right). Based on the results obtained, the fitted circle is assumed to be concentric with the coordinate system for all the flow conditions.

The average precession radius is obtained for the various discharge values by applying the above-mentioned method to the velocity fields obtained for the two horizontal measurement planes. The results are plotted in Fig. 10. Clearly, the precession radius is almost zero on both planes when $Q/Q_{\text{BEP}} = 0.91$, meaning that at this discharge the residual swirl exiting the runner forms a concentric vortex in the middle of the cone. The local swirl number in this case is not high enough for a distinct helical breakdown of the vortex. At $Q/Q_{\text{BEP}} = 0.87$, the vortex has a relatively small precession radius on the upper plane, which noticeably grows on the lower one. The amount of swirl at the runner exit is not high enough to trigger the helical instability. However, flowing downstream, the axial component of the velocity decreases due to the divergent geometry of the draft tube while its circumferential component remains almost constant. This increases the swirl number locally and initiates the breakdown of the vortex at a point between the upper and lower planes. For the three lower discharge values, the injected swirl is high enough so that the helical vortex breakdown occurs right at the runner exit, and therefore, r_{rope} is relatively high on both planes. The precession radius has a maximum at $Q/Q_{\text{BEP}} = 0.84$ and decreases gradually below this discharge. Recall that in the present experiments, UPLI is principally observed between 80 and 84% of the BEP discharge value, and the largest precession radii happen in this range as well.

Once the vortex centers have been determined, the spatial average of the tangential velocity profile (the tangential velocity as a function of distance from the vortex center) is obtained for each phase and then these averages are averaged over the entire precession cycle. An arbitrary radial coordinate system is first placed on the vertex center. All the measured tangential velocities at a given distance from the vortex center (r) are averaged over each 360° revolution to give the average velocity profiles per phase. The overall average and standard deviations are calculated over all the phases, the results of which are presented in Fig. 11 for the upper plane. As observed in Fig. 8, the vortices get closer to the draft tube wall as they flow downstream. This makes the 360° averaging method incapable of providing reliable results for the lower plane as a considerable proportion of the velocity vectors lie outside the confidence area. Hence, the tangential velocity profiles in Fig. 11 are only shown for the upper plane.

Figure 11 shows that as the discharge increases toward the BEP, the tangential velocity profile becomes more

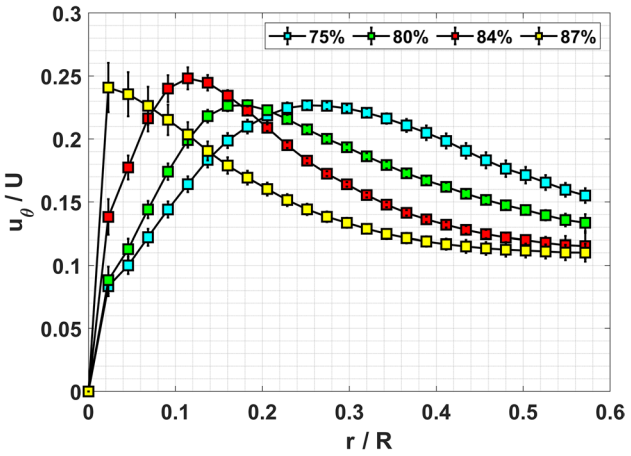

Fig. 11 Tangential velocity profiles obtained by spatial- and phase-averaging for different discharge values

concentrated with higher maximum tangential velocities and smaller viscous core radii. Note that the point [0, 0] is imposed on all the profiles. When $Q/Q_{\mathrm{BEP}} = 0.87$, the viscous core of the vortex is smaller than the measurement resolution, and thus, the maximum tangential velocity is not fully recovered in Fig. 11. As the discharge decreases, although the maximum tangential velocity of the vortex falls, a larger proportion of the sectional flow is forced to rotate around the vortex center at a higher velocity. It is noted that in Fig. 11, the error bars are multiplied by a factor of two to make them visible. Despite this magnification, the standard deviations remain very small, especially far from the vortex center, showing the reliability of the PIV measurements and the averaging algorithm used here. The higher errors close to the vortex core could be due to higher fluctuations in this area (actual flow fluctuations or induced by vortex wandering at each phase) or could be related to the limited number of valid vectors that were found at shorter distances from the vortex center.

The contours of the out-of-plane vorticity calculated from the PIV velocity fields by Eq. (8) are presented in Fig. 12. The contours clearly demonstrate how the flow patterns change on the different measurement planes (presented in rows) as the discharge increases from $Q/Q_{\mathrm{BEP}} = 0.75$ to 0.87 (presented in columns). The results can be interpreted in two ways: (1) the magnitude of the vorticity and (2) the area that is affected by the vortex rope in each section. Interestingly, by decreasing the discharge and going deeper into the part load, the magnitude of the maximum vorticity observed at the center of the vortex decreases. In contrast, the vortex-affected area grows and fills a much larger portion of the section at lower discharge values. This observation is in line with previous results that show that closer to the BEP, the vortex has a more concentrated structure with a lower impact

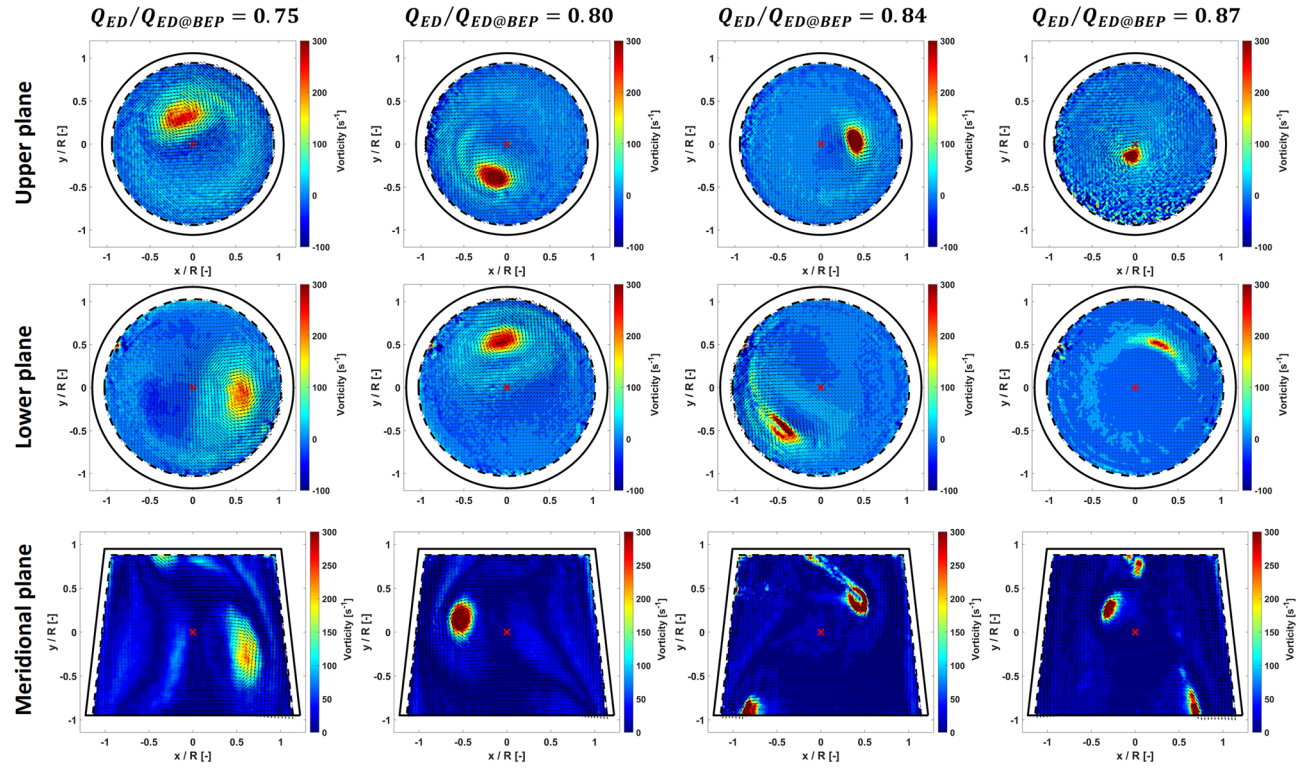

Fig. 12 Phase-averaged vorticity contours on the three measurement planes for four discharge values

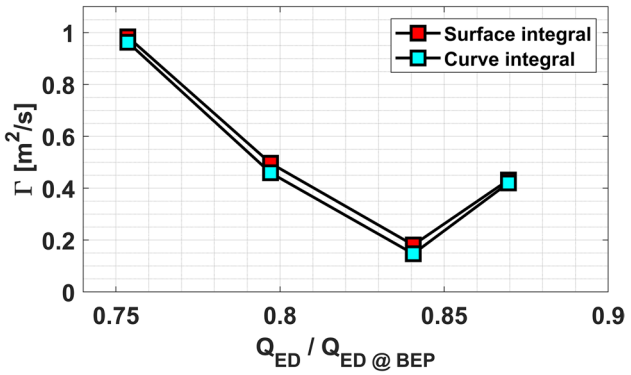

Fig. 13 Vortex intensity as a function of the discharge at nominal n_{ED}

on the surrounding flow. Moving farther downstream, the vortical structures become diffused in space and their maximum values are attenuated due to viscous diffusion.

To better compare the cases presented in Fig. 12, the contours of vorticity are further processed to extract the vortex intensity or circulation (Γ) for each case. This is achieved with the surface and curvilinear integrals detailed in Sect. 2. To this end, the area surrounding the vortex center, where the vortical flow is dominant, must be determined first. This is done with the second rule of Graftieaux's method (Graftieaux et al. 2001), where the variable Π_2 is calculated for the whole velocity field. In this method, a threshold of $\Pi_2 = 2/\pi$ denotes the boundary of the vortex. Once the vortex boundaries are delimited, its circulation can be calculated by the surface and curve integrals. The results of both methods are shown in Fig. 13 for the upper measurement plane. Being located close to the wall, it was not possible to close the vortex boundaries within the zone of the reliable velocity vectors on the lower plane of measurement. Consequently, these results are not included in Fig. 13.

Figure 13 shows that the two integrals both give almost the same values for the vortex intensity at each discharge. The trend is clear between $Q/Q_{\mathrm{BEP}} = 0.75$ and 0.84. The vortex intensity increases as the discharge is lowered. This is in line with the expectation, since a lower discharge is associated with a higher residual swirl injected into the draft tube. This swirl feeds up the vortex rope, and therefore, stronger vortices are expected. This is, however, in contrast with the results presented in Fig. 12 where the maximum value of the phase-averaged vorticity at $Q/Q_{\mathrm{BEP}} = 0.75$ is shown to be lower than in higher discharge values. This observation could be explained by the fact that the vortical flow is more dominant at $Q/Q_{\mathrm{BEP}} = 0.75$ and has larger boundaries (see Fig. 12), which ultimately leads to higher values of the integral parameter Γ presented in Fig. 13. Regarding the vortex intensity values obtained for the case of $Q/Q_{\mathrm{BEP}} = 0.87$ in Fig. 13, it is difficult to explain the observed jump. The value obtained could be physical or just an artifact of the measurements since the structure of the viscous core of the vortex was not fully captured for this discharge.

3.4 Effect of cavitation on the instability

The effect of Thoma number on UPLI is investigated in this section. Visualizations of the cavitation vortex rope in the draft tube are given in Fig. 14. The discharge is fixed at $Q/Q_{\mathrm{BEP}} = 0.84$ under nominal rotational velocity and nominal head. Initially, the Thoma number is $\sigma = 0.16$ and the vortex rope has a circular cross section. However, a slight decrease in the Thoma number to 0.14 triggers the UPLI and results in a drastic change in the shape of the vortex rope. At $\sigma = 0.14$, the vortex cross section has an elliptical shape and emits high-amplitude noise at frequencies higher than f_{rope} (studied in detail in Fig. 15). The high-speed visualizations clearly evidence that this trend continues. The elliptical shape of the vortex becomes more pronounced as the Thoma number is further decreased. This is accompanied by an increase in the amplitude of the pressure fluctuations induced by UPLI, as is shown in Amini et al. (2021). At lower values of σ (i.e., 0.08 and 0.06), the vortex rope loses its coherent shape and exhibits chaotic behavior with intermittent collapses and recoveries, which, in turn, reduce the amplitude of the UPLI-related pressure fluctuations, as evidenced in Amini et al. (2021).

Samples of the pressure signals recorded on the draft tube wall over a few revolutions of the runner at $\sigma = 0.16$ (black) and $\sigma = 0.12$ (red) are presented in Fig. 15 (left) for $Q/Q_{\mathrm{BEP}} = 0.84$. At $\sigma = 0.16$, the vortex undergoes simple precession. The minima of the curve represent the passage of the vortex in front of the pressure sensor. At $\sigma = 0.12$, there is a second source of high-frequency and high-amplitude fluctuations added to the initial precession. Clearly, UPLI is superimposed on the rotating vortex, and the high-frequency oscillations are modulated with the precession frequency. Still, the vortex passage can be detected by following the trend of the red curve and focusing on its absolute minimum in each period.

The power density spectrum of the pressure coefficient is depicted in Fig. 15 (middle) for the two signals measured under stable ($\sigma = 0.16$) and unstable ($\sigma = 0.12$) conditions at $Q/Q_{\mathrm{BEP}} = 0.84$. At the higher Thoma number, a distinct peak is obtained in the frequency domain at around $0.25f_{\mathrm{runner}}$, which corresponds to the precession frequency (f_{rope}). The second smaller peak of the black curve, which is close to the first one, is the first harmonic of the precession frequency. These two peaks are also present at the lower Thoma number. However, the occurrence of the instability at $\sigma = 0.12$ is associated with the appearance of an outstanding peak at $f_{\mathrm{upper}} \cong 2.8f_{\mathrm{runner}}$. The UPLI frequency is about 10 times higher than the precession frequency and its peak is even stronger in magnitude than that for the precession. A

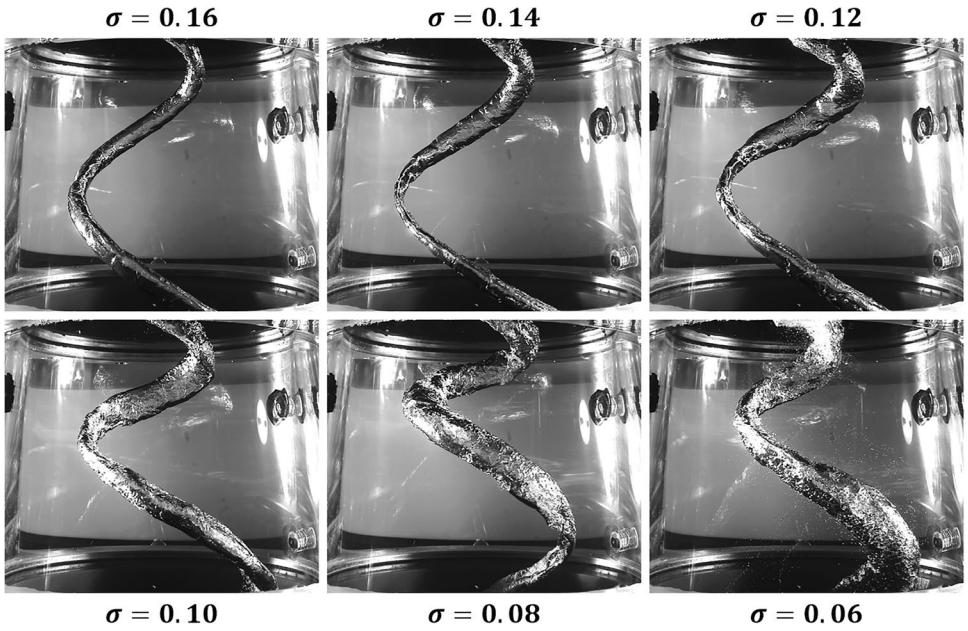

Fig. 14 Effect of Thoma number on the cavitation vortex rope and the occurrence of UPLI at nominal n_{ED} and $Q/Q_{\mathrm{BEP}} = 0.84$

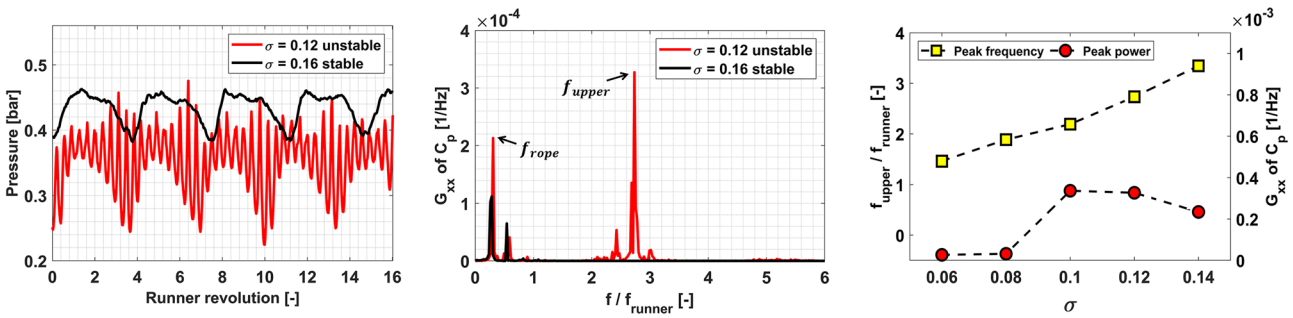

Fig. 15 Comparison of a simple precessing vortex and a vortex with UPLI. Left: Pressure signals in the time domain. Middle: Power density spectrum of the pressure coefficient. Right: Effect of Thoma number on UPLI peak frequency and power (measurements performed at nominal n_{ED} and $Q/Q_{\mathrm{BEP}} = 0.84$)

deeper look at the plot also reveals the existence of two side peaks around the UPLI frequency at $f_{\mathrm{upper}} \pm f_{\mathrm{rope}}$, which reflect the convective transfer mode of this instability with the precessing vortex, in line with previous studies (Koutnik et al. 2006; Favrel et al. 2019b).

The UPLI frequency and peak power are plotted in Fig. 15 (right) as functions of the Thoma number at $Q/Q_{\mathrm{BEP}} = 0.84$. It is clearly observed that f_{upper} decreases almost linearly as the Thoma number is reduced. A lower σ is associated with higher vapor volumes in the draft tube, which increases the flow compressibility and induces a decrease in the wave speed, and thus, in the eigenfrequencies of the system. Since UPLI occurs at an unstable eigenfrequency of the system (Dörfler 2019b), its frequency decreases as the cavitation volume increases. The peak power exhibits a more complex behavior. At the development phase of the instability, i.e., between its trigger at $\sigma = 0.14$ down to $\sigma = 0.10$, the power of the signal at f_{upper} increases as Thoma number is reduced, as illustrated in Fig. 14 (right). Lowering σ leads to a higher vapor volume and higher compressibility in the system, which, in turn, stores and releases higher amounts of energy in each cycle, resulting in higher signal power obtained at f_{upper}. At lower values of σ, however, the amplitude of the fluctuations at f_{upper} decreases, drastically. Namely, at $\sigma = 0.08$ and 0.06, the vortex loses its coherent shape due to the increased amount of cavitation, and consequently, the amplitude of the UPLI fluctuations decreases, as documented in Amini et al. (2021).

To better illustrate the effect of UPLI on pressure coefficients, the phase-averaged pressure profiles in cavitation-free ($\sigma = 0.48$), stable cavitation ($\sigma = 0.20$), and unstable cavitation ($\sigma = 0.09$) conditions are depicted in Fig. 16. These measurements are performed at a slightly lower discharge of $Q/Q_{\mathrm{BEP}} = 0.80$ at nominal n_{ED} and head. Obviously, the

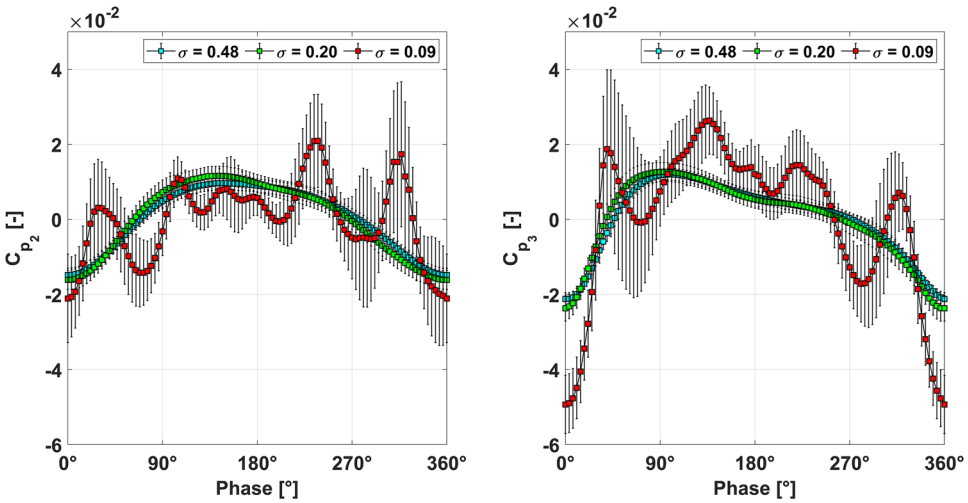

Fig. 16 Effect of σ on phase-averaged pressure profiles at the upper and lower measurement planes for the partial discharge $Q/Q_{\mathrm{BEP}} = 0.80$ and nominal n_{ED}

formation of a moderate amount of stable cavitation at the core of the vortex rope at $\sigma = 0.20$ does not influence the pressure coefficient measured at the draft tube wall. The only difference between these two flow conditions is the higher standard deviation values observed with cavitation present, about 60% higher on average. However, at $\sigma = 0.09$ (UPLI activated), the shape of the C_p profile completely alters. The precession is no longer the only dominant effect, and high-pitch high-amplitude fluctuations are superposed on it. As UPLI occurs, the standard deviation jumps to around 3.7 times that for $\sigma = 0.20$ on average.

It should be noted that for the unstable case in Fig. 16, as there are two dominant frequencies with similar powers in the pressure signal (precession motion and UPLI), the phase-averaging applied here could be contaminated with some sort of inaccuracy. The idea is, in fact, to divide the measurements into moments of the same phase based on the precession of the vortex. Thus, the minimum values in the pressure signal are chosen as the reference, as they indicate the passage of the vortex experienced by the sensor. However, in this case, the pressure fluctuations due to UPLI are strong enough to alter the pressure signal significantly. Thus, the minimum values detected do not necessarily correspond to the exact moment of the vortex passing by the sensor. As f_{upper} is not an integer product of f_{rope} in general, this leads to some level of inaccuracy in the phase-averaged signals. For instance, as shown in Fig. 16, the sub-cycle oscillations do not occur at a fixed frequency equal to f_{upper}. The purpose of the results presented in Fig. 16 is, thus, to provide the readers with a qualitative comparison between the stable and unstable cases in terms of phase-averaged signal amplitude and contamination.

The phase-averaged velocity and vorticity contours of the cavitation-free flow as well as the two stable and unstable cavitation states measured on the upper PIV plane are presented in Fig. 17. The turbine discharge is fixed at $Q/Q_{\mathrm{BEP}} = 0.80$, and nominal n_{ED} is maintained. Obviously, the occurrence of cavitation partly blocks the acquired PIV images, and thus, the obtained contours include some useless areas where, instead of the velocity field on the measurement plane, only a reflection of the cavitation body of the vortex rope is captured.

In Fig. 17, the phase-averaged velocity and vorticity contours of cavitation-free flow at $\sigma = 0.48$ are presented on the left, whereas the results shown in the middle and right correspond to cavitation conditions. At $\sigma = 0.20$, the cavitation vortex rope is stable with a circular cross section. At $\sigma = 0.09$, UPLI occurs, and the vortex rope is elliptical. The contours presented in Fig. 17 clearly show that at $Q/Q_{\mathrm{BEP}} = 0.80$, which has been shown to be quite susceptible to UPLI occurrence, the vortex rope originally holds a circular cross section in cavitation-free flow; and it is only through the diminution of the cavitation number below a certain threshold that the instability is triggered and the vortex section turns elliptical. It is also observed that the vortex is well defined in the cavitation-free flow, and the vorticity contour clearly depicts the vortex core where viscous effects are dominant.

At $\sigma = 0.20$, a considerable amount of vapor is already present in the vortex core. The contours shown in Fig. 17, however, suggest that the occurrence of cavitation within the core of the vortex rope, as long as it remains circular, does not modify the velocity or vorticity field drastically. It seems that the viscous core of the vortex is moderately enlarged due to cavitation, and as a result, the maximum tangential velocity and the maximum vorticity measured close to the edges of the cavitation core are slightly diminished. It is more difficult to compare the result at $\sigma = 0.09$ with the two other situations, as the cavitation vortex rope is quite large and blocks a considerable part of the view. However, it may

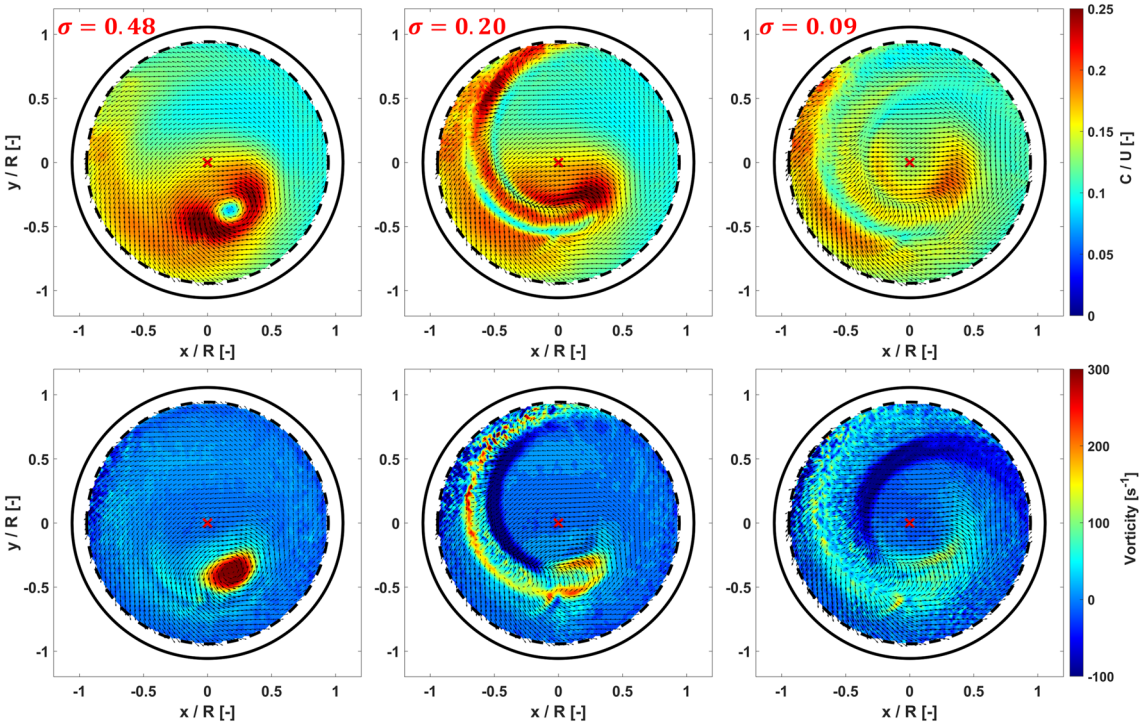

Fig. 17 Phase-averaged contours of velocity magnitude (top) and vorticity (bottom) obtained on the upper plane for three different values of Thoma number at $Q/Q_{\mathrm{BEP}} = 0.80$ and nominal n_{ED}

still be inferred that the velocity field is more diffused at this Thoma number and that the maximum tangential velocity adjacent to the vortex core is significantly diminished.

It should be recalled that the observed diffusion effect in the velocity and vorticity fields at $\sigma = 0.09$ in Fig. 17 may partially stem from the aforementioned effect of phase-averaging that occurs for UPLI due to large-amplitude pressure fluctuations. To get a better insight of the flow field in the presence of cavitation within the vortex rope, three contours of instantaneous velocity fields are shown in Fig. 18. The corresponding PIV images are also presented so that the readers can have a clear view of the position and size of the cavitation vortex. As the vortex has a circular cross section at $\sigma = 0.20$, only one instant of the flow field is presented for this Thoma number. The occurrence of UPLI, however, results in a self-rotating elliptical vortex. Therefore, for $\sigma = 0.09$, two moments at which the vortex is at the same phase of precession are presented. The first PIV image is taken when the smaller diameter of the ellipse faces the camera, whereas in the second image, the larger diameter is visible. This allows one to compare the velocity fields obtained on the two sides of the elliptical vortex core.

It is noted that all the PIV images of circular vortices have almost the same shape as the one in Fig. 18 (left). However, this does not hold for the elliptical vortices, and two completely different states may be observed, depending on whether the shorter or larger diameter of the ellipse faces the PIV camera. It is clear in Fig. 18 (middle) that the velocity field surrounding the sharper edge of the ellipse strongly resembles that of the circular vortex (the left contour), in terms of both magnitude and distribution pattern. In contrast, when the larger diameter of the ellipse faces the camera, the velocity field alters so that the magnitude of the circumferential velocity is significantly lower close to the vortex core and higher at farther locations. This makes it apparent that, for the elliptical vortex, the state of the flow is not fully described by the precession phase, and therefore, the phased-averaged velocity fields are not high-fidelity representations of the flow.

The ensemble of the observations in this paper suggests that the occurrence of UPLI strongly depends on the cavitation volume inside the core of a precessing vortex. For each given flow condition, the vortex becomes unstable once the cavitation volume surpasses a certain threshold. So far, this has been achieved by fixing Fr and n_{ED} at their nominal values and gradually reducing σ at a given discharge. Now, the effect of the distribution of the cavitation volume on UPLI is evaluated by changing the Froude number. The corresponding results are shown in Fig. 19, where the flow conditions are fixed at $Q/Q_{\mathrm{BEP}} = 0.87$, $\sigma = 0.06$, and nominal n_{ED}, whereas Fr is varied by changing the turbine head. At nominal Froude number (Fr = 7.75), UPLI does not occur at this high discharge (87% of BEP), even for a σ as low as 0.06. Interestingly, it is observed that UPLI can be activated

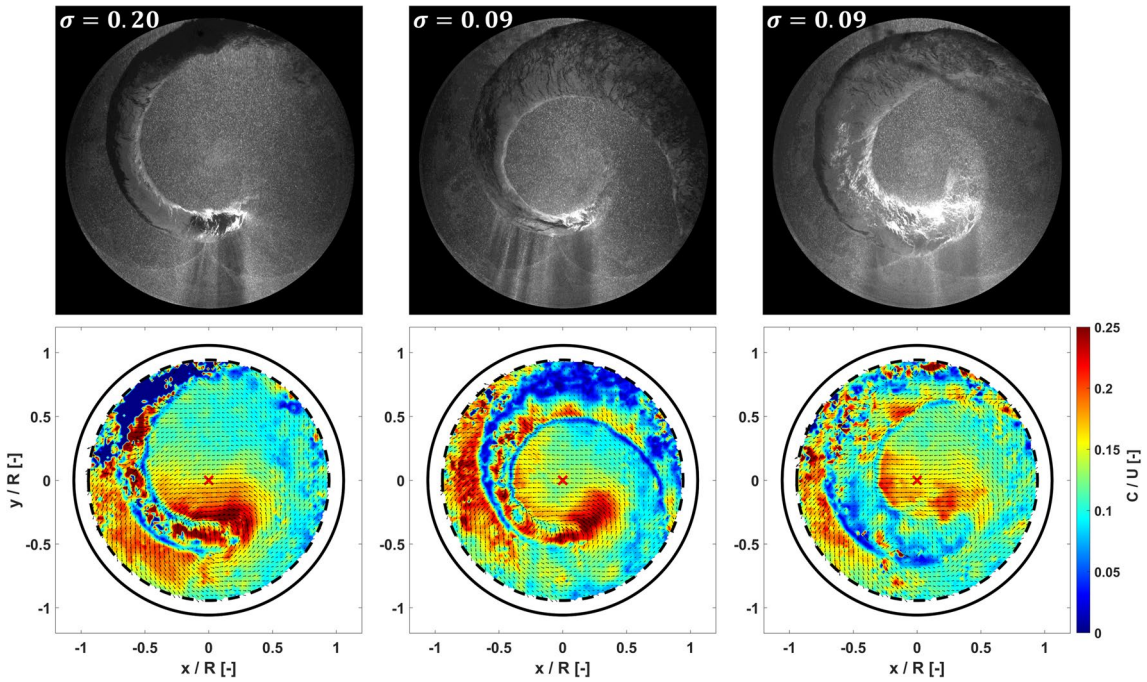

Fig. 18 PIV images along with their corresponding instantaneous velocity fields obtained on the upper measurement plane for different values of Thoma number at $Q/Q_{\mathrm{BEP}} = 0.80$

Fig. 19 Influence of Froude number on the cavitation vortex rope and the occurrence of UPLI. Measurements are performed at nominal n_{ED}, $\sigma = 0.06$, and $Q/Q_{\mathrm{BEP}} = 0.87$

by increasing the Froude number to Fr = 9.10. This observation is in agreement with Nicolet et al.'s findings (Nicolet et al. 2010), which shows that UPLI is more likely to occur in models compared to prototypes as the Froude number is normally higher for the former. An increase in the Froude number is known to lead to thinner but longer cavitation vortices in the draft tube for a fixed Thoma number. This observation clearly evidences that it is not only the total cavitation volume but also its distribution along the draft tube that plays a pivotal role in the initiation and development of UPLI.

4 Discussion: root cause analysis of UPLI

Considering the presented results, two principal questions arise on the nature of this instability: (1) Why is this phenomenon associated with large-amplitude pressure fluctuations? (2) What is the driving force that activates this unstable mode?

Regarding the first question, Koutnik et al. (2006) and Kirschner et al. (2009) attribute the UPLI-induced pressure fluctuations at f_{upper} to the self-rotation of a vortex rope with an elliptical shape. They believe that the rotation of an asymmetric velocity field about the vortex axis, which is also highlighted by our PIV results in Sect. 3, creates an alternating pressure field. Although relevant, this theory is

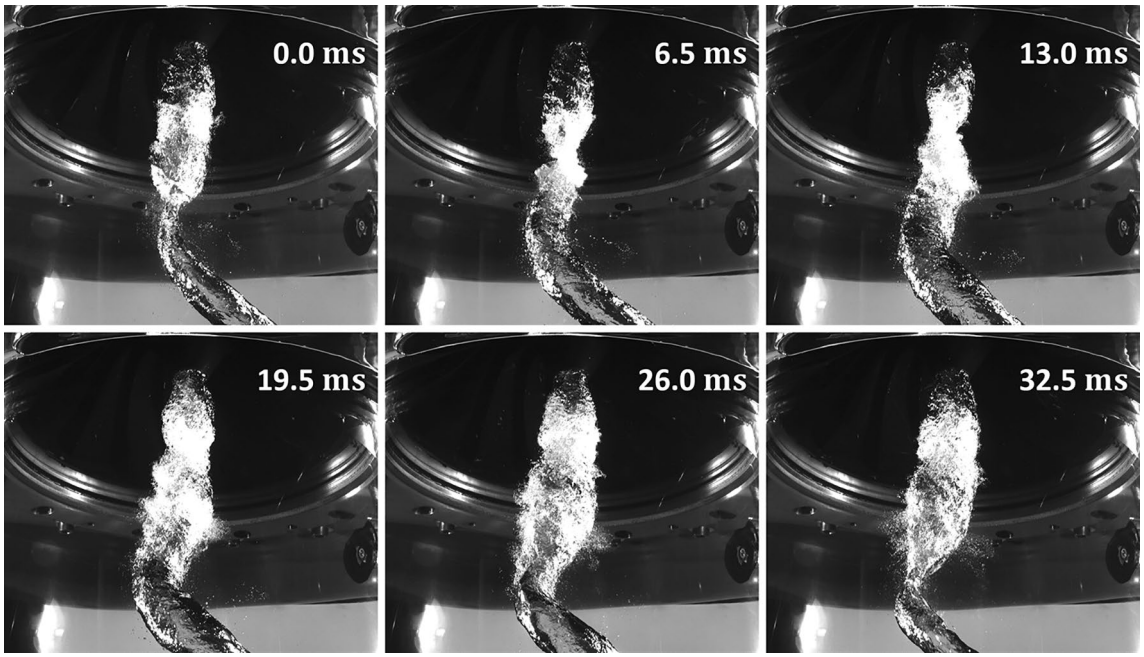

Fig. 20 Breathing mechanism observed at the upper part of the vortex rope connected to the runner hub. The operating conditions are nominal n_{ED}, Fr = 9.10, $\sigma = 0.06$, and $Q/Q_{\mathrm{BEP}} = 0.87$

not consistent with the synchronous nature of these fluctuations. In contrast, Nicolet et al. (2010) and Dörfler (2019b) consider that a breathing mode is the source of these fluctuations. In this regard, a sequence of images extracted from high-speed flow visualizations depicting the root of the cavitation vortex rope at nominal n_{ED}, $Q/Q_{\mathrm{BEP}} = 0.87$, $Fr = 9.10$, and $\sigma = 0.06$ are shown in Fig. 20. These flow visualizations clearly reveal that there is a periodic increase and decrease in the vapor volume (with period T) at the upper part of the precessing vortex where it attaches to the turbine hub. This implies the existence of the so-called breathing mechanism. The period of these volume oscillations exactly matches f_{upper}, which proves that the UPLI-induced pressure pulsations and the cavitation volume oscillations are strongly interconnected and both fluctuate at (probably) one of the systems eigenfrequencies, which can explain the synchronous nature of these fluctuations.

To determine the origin of this instability, we can refer to the governing principles of swirling flows. In these flows, as the swirl number, roughly defined as the ratio of the angular momentum to the axial momentum, exceeds certain critical thresholds, the flow undergoes a sequence of instabilities. As shown in Ruith et al. (2003), this sequence includes bubbling, helical, and double-helical modes. A precessing vortex rope has already experienced the bubbling (the inflated part attached to the hub) and helical breakdowns. A further increase in the swirl number of the flow in the draft tube pushes the vortex toward the double-helical breakdown, which is associated with two co-rotating vortical braids that create an elliptical cross section, as is also observed with UPLI.

It has been shown in this paper that UPLI occurs when the vapor volume in the core of the vortex exceeds a critical value. The center of the vortex holds vapor whose angular momentum is negligible compared to that of the liquid phase. Therefore, as the cavitation volume increases within the vortex core, the remaining swirl that leaves the runner must be distributed over a lower surface area and at larger radii. This hypothesis suggests that an increase in the cavitation volume could lead to an increase in the local swirl number, which, in turn, may trigger the double-helix breakdown mode. The evidence for the occurrence of this phenomenon for UPLI is presented in Fig. 21. The sequence of images illustrates the partial collapse of the cavitation core of the vortex rope at nominal n_{ED}, $Q/Q_{\mathrm{BEP}} = 0.84$, and $\sigma = 0.10$. As is clear in the fifth picture (24 ms), two cavitation braids remain on the two sides of the elliptical vortex during the partial collapse. A deeper look at the high-speed video of Fig. 21 (provided as supplementary material) reveals that these two side structures are co-rotating vortices, which strengthens the theory for a vortex breakdown. This observation is in good agreement with recent studies (Favrel et al. 2019b) and shows that the elliptical cavitation vortex is, in fact, made of two smaller cavitation vortices, the space between which is filled with vapor due to low pressures between the two braids. A rise in pressure (due to the oscillations induced by the breathing mechanism) results in the removal of

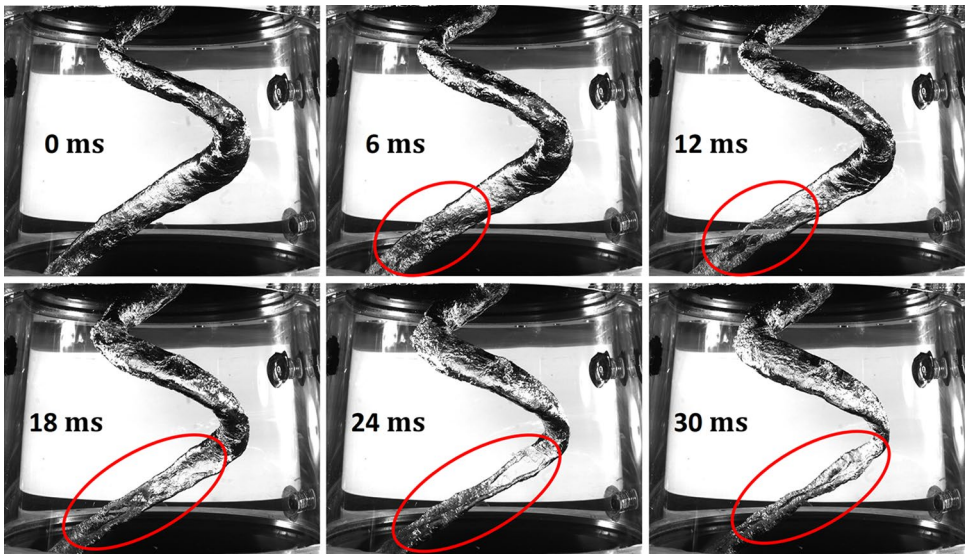

Fig. 21 Occurrence of the double-helical vortex breakdown and the emergence of two co-rotating vortex cores. The flow conditions are nominal n_{ED}, $Q/Q_{\mathrm{BEP}} = 0.84$, and $\sigma = 0.10$

vapor at the center of the elliptical vortex, while the two side vortices continue to cavitate due to lower pressures created by the rotational motion. This observation and analysis suggest that the elliptical shape of the vortex rope at UPLI is most likely the result of an increased swirl number due to an augmented cavitation volume in the draft tube. The double-helical breakdown may occur at the runner outlet or farther downstream, leading to the formation of an elliptical cavitation vortex rope. Further research is required to prove this theory and determine which of the influencing parameters plays the most critical role in the activation of UPLI in Francis turbines.

The analysis on the origin of the UPLI would not be complete without discussing the possible effects of dissolved gases. Although not investigated explicitly in the present study, it is believed that the air content should play a role in the initiation and development of UPLI. In fact, it has been shown here that the instability threshold of UPLI strongly depends on the cavitation volume. For a fixed operating point, a change in the air content is expected to alter (even slightly) the size of the cavitation core of the vortex. As a higher gas content results in a larger cavitation volume due to diffusion effects (Amini et al. 2019a), it can potentially shift the instability toward higher Thoma numbers. Moreover, a higher amount of non-condensable gases in the cavitation vortex changes its compressibility, which, in turn, influences the system eigenfrequencies. Consequently, the breathing frequency of the UPLI, which is believed to match one of the system eigenfrequencies, should change accordingly. Further studies are required to confirm these assumptions and investigate them in detail.

5 Conclusion

In this paper, the UPLI is investigated experimentally for a reduced-scale model Francis turbine. It is known that UPLI may occur in medium- and high-specific-speed Francis turbines at discharge values between 70 and 85% of the BEP. This instability, in which the vortex rope has an elliptical shape, is accompanied by large-amplitude pressure fluctuations emitted at a distinct high frequency between 2 and 4 times the runner rotational speed. These fluctuations induce strong vibrations in the hydraulic circuit and negatively impact the machine performance and health.

A significant number of tests are conducted on operating points featuring UPLI, both in cavitation-free and cavitation flows, to delimit the instability ranges, to identify its driving forces, and to clarify its impacts on the draft tube flow. The measurements performed in cavitation-free conditions clearly demonstrate that the precession frequency of the vortex rope as well as the power of this frequency in the spectrum increase significantly at operating points susceptible to UPLI. This is a key finding, as such behavior is not observed for other Francis turbines that do not suffer from this type of instability (Favrel et al. 2015). This pattern could be used as an indicator to evaluate the risk of UPLI. Further measurements on other machines are necessary before generalizing this statement, though.

Moreover, the velocimetry results clearly show that the flow pattern in the draft tube is identical for all the cavitation-free part-load cases (with UPLI or not). The vortex rope has a circular cross section as long as there is no cavitation within its core. PIV results for cavitation-free conditions demonstrate that the operating points most susceptible to UPLI (in this case, 80% and 84% of the BEP discharge) have very concentrated vortical structures and show the largest

precession radii within the measured range. Although they have smaller circulation values, their compact viscous cores lead to larger maximum tangential velocities and higher vorticities at their centers. The instantaneous velocity fields obtained during UPLI in the presence of cavitation reveal that the flow is not symmetric around the elliptical core of the vortex rope and higher velocities are observed along the sharper edges of the ellipse.

It is also evidenced that the occurrence of UPLI strongly depends on the cavitation volume within the precessing vortex rope. Above the instability threshold, the vortex is circular and stable. Decreasing the Thoma number leads to an abrupt change in the flow regime by triggering UPLI while the vortex cross section transforms into an ellipse. In addition, it has been shown that f_{upper} decreases constantly as σ is reduced while its power first experiences a rise and then a sudden drop, which is probably due to the loss of coherence in the flow caused by excessive amounts of cavitation. The existence of a breathing mode in this instability is proven with high-speed flow visualizations. The videos also highlight the development of two side vortices on the sharp edges of the elliptical vortex, which gives rise to the hypothesis that UPLI is the next episode in the instability sequence of swirling flows after a helical breakdown. This suggests that the amount of swirl increases in the draft tube as the Thoma number is reduced. Once it exceeds a critical threshold, the double-helix mode is activated.

The results presented in this paper provide a much deeper insight into the flow structures that favor the UPLI occurrence as well as its impact on the draft tube flow and help delimit its thresholds to higher precision, which can be used to prevent UPLI during turbine operation. These findings can also be used to enhance theoretical and numerical modeling of this phenomenon in Francis turbines. Further investigations are still required to improve our understanding of this instability. One of the remaining questions is the possible role that air content may play in the initiation and development of UPLI. The study of the match between the UPLI breathing frequency and one of the system eigenfrequencies as well as how one can transpose UPLI results of model tests to prototype are other important topics to investigate regarding this phenomenon.

Supplementary Information The online version contains supplementary material available at https://doi.org/10.1007/s00348-023-03649-0.

Acknowledgements The authors are thankful to Nippon Koei Co., Ltd. (Japan) for making the reduced-scale model available for tests.

Author contributions All authors contributed to the study conception and design. AA and EV prepared the material and carried out the experiments. AA performed the post-processing and generated the figures. EV and AF contributed to the analysis and discussion of the results. AM and KY provided overall guidance. FA supervised the project and secured funds. The first draft of the manuscript was written by AA. All authors read and approved the final manuscript.

Funding Open access funding provided by EPFL Lausanne. This research was funded by the Swiss Federal Office of Energy through the project POST (Grant No. SI/501943-01).

Data availability The data that support the findings of this study are available from the corresponding author upon reasonable request.

Declarations

Conflict of interest The authors declare that they have no conflict of interest.

Ethical approval Not applicable.

References

Alligné S, Nicolet C, Avellan F (2011) Identification by CFD simulation of the mechanism inducing upper part load resonance phenomenon. In: Proceedings of the 4th international meeting on cavitation and dynamic problems in hydraulic machinery and systems, Belgrade, Serbia

Amini A, Reclari M, Sano T et al (2019a) On the physical mechanism of tip vortex cavitation hysteresis. Exp Fluids 60:118. https://doi.org/10.1007/s00348-019-2762-x

Amini A, Reclari M, Sano T et al (2019b) Suppressing tip vortex cavitation by winglets. Exp Fluids 60:159. https://doi.org/10.1007/s00348-019-2809-z

Amini A, Seo J, Rhee SH, Farhat M (2019c) Mitigating tip vortex cavitation by a flexible trailing thread. Phys Fluids 31:127103. https://doi.org/10.1063/1.5126376

Amini A, Vagnoni E, Favrel A et al (2021) An experimental study on the upper part-load elliptical vortex instability in a Francis turbine. IOP Conf Ser Earth Environ Sci 774:012002. https://doi.org/10.1088/1755-1315/774/1/012002

Arabnejad MH, Amini A, Farhat M, Bensow RE (2020) Hydrodynamic mechanisms of aggressive collapse events in leading edge cavitation. J Hydrodyn 32:6–19. https://doi.org/10.1007/s42241-020-0002-8

Arpe J, Nicolet C, Avellan F (2009) Experimental evidence of hydroacoustic pressure waves in a Francis turbine elbow draft tube for low discharge conditions. J Fluids Eng 131:081102

Avellan F (2004) Introduction to cavitation in hydraulic machinery, In: Proceedings of the 6th International conference on hydraulic machinery and hydrodynamics, invited paper HMH2004, Timisoara, Romania, October 21–22

Cala CE, Fernandes EC, Heitor MV, Shtork SI (2006) Coherent structures in unsteady swirling jet flow. Exp Fluids 40:267–276. https://doi.org/10.1007/s00348-005-0066-9

Dörfler PK (1994) Observation of the pressure pulsation on Francis model turbine with high specific speed. Hydropower & Dams 21–26

Dörfler PK (2019a) Analysis of the Francis turbine upper-part-load pulsation Part I—experimental results versus hydro-acoustic model. IOP Conf Ser Earth Environ Sci 240:052022. https://doi.org/10.1088/1755-1315/240/5/052022

Dörfler PK (2019b) Analysis of the Francis turbine upper-part-load pulsation Part II—mechanism of self-excitation. IOP Conf Ser Earth Environ Sci 240:052023. https://doi.org/10.1088/1755-1315/240/5/052023

Dreyer M, Decaix J, Münch-Alligné C, Farhat M (2014) Mind the gap: a new insight into the tip leakage vortex using stereo-PIV. Exp Fluids 55:1849. https://doi.org/10.1007/s00348-014-1849-7

Escaler X, Egusquiza E, Farhat M et al (2006) Detection of cavitation in hydraulic turbines. Mech Syst Signal Process 20:983–1007. https://doi.org/10.1016/j.ymssp.2004.08.006

Favrel A, Müller A, Landry C et al (2015) Study of the vortex-induced pressure excitation source in a Francis turbine draft tube by particle image velocimetry. Exp Fluids 56:215. https://doi.org/10.1007/s00348-015-2085-5

Favrel A, Müller A, Landry C et al (2016) LDV survey of cavitation and resonance effect on the precessing vortex rope dynamics in the draft tube of Francis turbines. Exp Fluids 57:168. https://doi.org/10.1007/s00348-016-2257-y

Favrel A, Gomes Pereira Junior J, Landry C et al (2019) Dynamic modal analysis during reduced scale model tests of hydraulic turbines for hydro-acoustic characterization of cavitation flows. Mech Syst Signal Process 117:81–96. https://doi.org/10.1016/j.ymssp.2018.07.053

Favrel A, Liu Z, Takahashi W et al (2019) Visualization of the elliptical form of a cavitation vortex rope and its collapse by two cameras. IOP Conf Ser: Earth Environ Sci 405:012035. https://doi.org/10.1088/1755-1315/405/1/012035

Favrel A, Liu Z, Khozaei MH et al (2022) Anti-phase oscillations of an elliptical cavitation vortex in Francis turbine draft tube. Phys Fluids 34:064112. https://doi.org/10.1063/5.0091210

Fisher RK, Palde U, Ulith P (1980) Comparison of draft tube surging of homologous scale models and prototype Francis turbines. In: Proceeding of the 10th IAHR symposium on hydraulic machinery and systems (Tokyo, 1980). pp 541–556

Gawandalkar U, Poelma C (2022) The structure of near-wall re-entrant flow and its influence on cloud cavitation instability. Exp Fluids 63:77. https://doi.org/10.1007/s00348-022-03417-6

Gomes Pereira J, Vagnoni E, Favrel A et al (2022) Prediction of unstable full load conditions in a Francis turbine prototype. Mech Syst Signal Process 169:108666. https://doi.org/10.1016/j.ymssp.2021.108666

Goyal R, Gandhi BK (2018) Review of hydrodynamics instabilities in Francis turbine during off-design and transient operations. Renew Energy 116:697–709. https://doi.org/10.1016/j.renene.2017.10.012

Goyal R, Cervantes MJ, Gandhi BK (2017) Vortex rope formation in a high head model francis turbine. J Fluids Eng. https://doi.org/10.1115/1.4035224

Goyal R, Gandhi BK, Cervantes MJ (2017) Experimental study of mitigation of a spiral vortex breakdown at high Reynolds number under an adverse pressure gradient. Phys Fluids 29:104104. https://doi.org/10.1063/1.4999123

Graftieaux L, Michard M, Grosjean N (2001) Combining PIV, POD and vortex identification algorithms for the study of unsteady turbulent swirling flows. Meas Sci Technol 12:1422–1429. https://doi.org/10.1088/0957-0233/12/9/307

Joy J, Raisee M, Cervantes MJ (2022) A novel guide vane system design to mitigate rotating vortex rope in high head Francis model turbine. Int J Fluid Mach Syst 15:188–209

Khullar S, Singh KM, Cervantes MJ, Gandhi BK (2022) Numerical analysis of water jet injection in the draft tube of a Francis turbine at part load operations. J Fluids Eng. https://doi.org/10.1115/1.4054564

Kirschner O, Ruprecht A, Göde E (2009) Experimental investigation of pressure pulsation in a simplified draft tube. In: Proceedings of the 3rd IAHR international meeting of the workgroup on cavitation and dynamic problems in hydraulic machinery and systems, Brno, Czech Republic. Citeseer, pp 55–65

Kougias I, Aggidis G, Avellan F et al (2019) Analysis of emerging technologies in the hydropower sector. Renew Sustain Energy Rev 113:109257. https://doi.org/10.1016/j.rser.2019.109257

Koutnik J, Krüger K, Pochyly F, et al (2006) On cavitating vortex rope form stability during Francis turbine part load operation. In: Proceedings of the first meeting of the IAHR Int. Working Group on Cavitation and Dynamic Problems in Hydraulic Machinery and Systems (Barcelona)

LiRen DZ, Yu L et al (2021) Spatio-temporal evolution mechanism of cavitation vortex ropes in a swirling flow. Phys Fluids 33:104107. https://doi.org/10.1063/5.0067735

Müller A, Dreyer M, Andreini N, Avellan F (2013) Draft tube discharge fluctuation during self-sustained pressure surge: fluorescent particle image velocimetry in two-phase flow. Exp Fluids 54:1514. https://doi.org/10.1007/s00348-013-1514-6

Müller A, Favrel A, Landry C, Avellan F (2017) Fluid–structure interaction mechanisms leading to dangerous power swings in Francis turbines at full load. J Fluids Struct 69:56–71. https://doi.org/10.1016/j.jfluidstructs.2016.11.018

Nicolet C, Zobeiri A, Maruzewski P, Avellan F (2010) On the upper part load vortex rope in Francis turbine: experimental investigation. IOP Conf Ser Earth Environ Sci 12:012053. https://doi.org/10.1088/1755-1315/12/1/012053

Pasche S, Gallaire F, Avellan F (2018) Predictive control of spiral vortex breakdown. J Fluid Mech 842:58–86

Pasche S, Avellan F, Gallaire F (2019) Optimal control of part load vortex rope in Francis turbines. J Fluids Eng. https://doi.org/10.1115/1.4042560

Pasche S, Gallaire F, Avellan F (2019b) Origin of the synchronous pressure fluctuations in the draft tube of Francis turbines operating at part load conditions. J Fluids Struct 86:13–33

Rivetti A, Angulo M, Lucino C, Liscia S (2015) Pressurized air injection in an axial hydro-turbine model for the mitigation of tip leakage cavitation. J Phys Conf Ser 656:012069. https://doi.org/10.1088/1742-6596/656/1/012069

Ruith MR, Chen P, Meiburg E, Maxworthy T (2003) Three-dimensional vortex breakdown in swirling jets and wakes: direct numerical simulation. J Fluid Mech 486:331–378. https://doi.org/10.1017/S0022112003004749

Sreedhar BK, Albert SK, Pandit AB (2017) Cavitation damage: theory and measurements—a review. Wear 372–373:177–196. https://doi.org/10.1016/j.wear.2016.12.009

International Electrotechnical Commission (1999) Hydraulic turbines, storage pumps and pump-turbines—model acceptance tests. IEC International Standard IEC 60193:2019–04

Teran LA, Rodríguez SA, Laín S, Jung S (2018) Interaction of particles with a cavitation bubble near a solid wall. Phys Fluids 30:123304. https://doi.org/10.1063/1.5063472

Wack J, Riedelbauch S (2015) Numerical simulations of the cavitation phenomena in a Francis turbine at deep part load conditions. J

Phys Conf Ser 656:012074. https://doi.org/10.1088/1742-6596/656/1/012074

Yamamoto K, Müller A, Favrel A, Avellan F (2017) Experimental evidence of inter-blade cavitation vortex development in Francis turbines at deep part load condition. Exp Fluids 58:142. https://doi.org/10.1007/s00348-017-2421-z

Zhao W, Presas A, Egusquiza M et al (2021) Increasing the operating range and energy production in Francis turbines by an early detection of the overload instability. Measurement 181:109580. https://doi.org/10.1016/j.measurement.2021.109580